# **Empirical Characterization of a High-performance Exterior-rotor Type Brushless DC Motor and Drive**

Ung Hee Lee, Student Member, IEEE, Chien-Wen Pan, Elliott J. Rouse, Member, IEEE

Abstract—Recently, brushless motors with especially high torque densities have been developed for applications in autonomous aerial vehicles (i.e. drones), which usually employ exterior rotor-type geometries (ER-BLDC motors). These motors are promising for other applications, such as humanoids and wearable robots; however, the emerging companies that produce motors for drone applications do not typically provide adequate technical specifications that would permit their general use across robotics—for example, the specifications are often tested in unrealistic forced convection environments, or are drone-specific, such as thrust efficiency. Furthermore, the high magnetic pole count in many ER-BLDC motors restricts the brushless drives able to efficiently commutate these motors at speeds needed for lightly-geared operation. This paper provides an empirical characterization of a popular ER-BLDC motor and a new brushless drive, which includes efficiencies of the motor across different power regimes, identification of the motor transfer function coefficients, thermal response properties, and closed loop control performance in the time and frequency domains. The intent of this work is to serve as a benchmark and reference for other researchers seeking to utilize these exciting and emerging motor geometries.

Index Terms—Brushless Motors, Wearable Robots, Drones, Actuator Design, Electromechanics

## I. Introduction

The usage of electric motors in autonomous aerial vehicles (i.e. drones) has advanced the proliferation of new brushless motor sizes and geometries that may have important implications in other areas of robotics. These motor geometries were developed to provide the high torque required for drone applications, without the need for a transmission. Transmissions are often undesirable because they universally add weight and audible noise, as well as reduce the system's efficiency and specific power-concepts which are especially important for drones and other applications, such as wearable robots. Consequently, motor manufacturers have expanded the availability of high torque exterior-rotor type (ER-) BLDC motors, which can be used in direct drive implementations for autonomous aerial vehicles. These ER-BLDC motors are usually larger in diameter, ranging from  $2\sim 11$  cm in diameter, while only being  $1\sim 2$  cm in axial

This work was supported by the NSF National Robotics Initiative (NRI) under Grant No. CMMI 1734586.

length. The large diameter stems from the substantial torque that can be required, as motor torque is proportional to the square of the radius.

The development and usage of ER-BLDC motors in the drone industry have outpaced rigorous electromechanical characterization of the motors and associated drives. These motors have gained popularity due to their low cost and high performance; however, obtaining specifications for these motors can be challenging. With the exception of a few research groups that study the implementation of ER-BLDC motors in robotic applications [1]-[3], the motor specifications that can be obtained are often sparse, result from unrealistic testing conditions, or in units that are specific to drone applications (e.g. thrust efficiency). Furthermore, ER-BLDC motors utilized in drone applications implement openloop commutation systems, known as 'electronic speed controllers' (ESCs). These ESCs cannot operate at low speeds, and thus are not appropriate for wearable robotics tasks (e.g. locomotion). In addition, many common commerciallyavailable BLDC drives cannot efficiently commutate some ER-BLDC motors, and more specialized options must be used. The high number of pole pairs causes an increase in the transition rate between motor windings, which can exceed the computational limitations of modern BLDC drives [4]. Fortunately, new drive systems have been developed specifically to commutate the high number of pole pairs in some ER-BLDC motors at speeds required for some applications [5]. However, a rigorous, empirical characterization of these motors and drives is yet to be completed.

In this paper, we performed an empirical electromechanical characterization of a new ER-BLDC motor (T-motor U8-KV100, Nanchang, Jiangxi, China), originally created for the drone industry. In addition, our characterization provides insight into the performance of a recently-developed brushless drive (model: Dephy Actuator Package (DAP), Dephy Inc., Maynard, MA, USA) capable of efficiently commutating the high number of pole pairs (N=21). The main contributions of this paper are the complete characterization of a popular ER-BLDC motor and accompanying drive, which will serve as a benchmark for use of these motors in wearable robotic applications; the characterization included identification of the motor's transfer function coefficients (e.g. torque / back-EMF constants, rotor inertia, and viscous damping parameters), the empirically-determined efficiencies across a range of torque-speed regimes, the thermal response properties, and the closed-loop control performance in the time and frequency domains.

U. Lee and E. J. Rouse are with the Department of Mechanical Engineering and the Robotics Institute, University of Michigan, Ann Arbor, MI 48109 USA, and also with the Neurobionics Lab, University of Michigan, Ann Arbor, MI 48109 USA (email: unghee@umich.edu, ejrouse@umich.edu).

C. Pan was with the Robotics Institute, University of Michigan, Ann Arbor, MI 48109 USA, and also with the Neurobionics Lab, University of Michigan, Ann Arbor, MI 48109 USA, and now with the Human-Oriented Robotics and Control Lab, Department of Mechanical and Aerospace Engineering, Arizona State University, Tempe, AZ 85287 USA (email: cpan22@asu.edu).

#### II. CHARACTERIZATION METHODS

This study focuses on the empirical characterization of a popular ER-BLDC motor that has had recent success in autonomous robotic applications, namely the T-motor U8-KV100 (Nanchang, Jiangxi, China) [2], [6]-[10]. To this end, we investigated two versions of the U8-KV100; the first version was the unmodified U8-KV100, and the second version included a custom modified housing, which facilities use in our application area of interest (e.g. wearable robotics). The modified U8-KV100 was designed by Dephy Inc., and is slightly lighter (230 g vs. 240 g) and substantially thinner (17 mm vs. 26 mm) than the standard U8-KV100. Both motor versions have a diameter of 87 mm and the electromagnetic properties of the motors are identical. The brushless drive used in this study was also developed by Dephy Inc., and is based on the open-source Flexible, Scalable Electronics Architecture (FlexSEA) project developed for wearable robotics applications [5]. The custom modified U8-KV100 motor, coupled to a commercial version of the FlexSEA brushless drive, are known together as the Dephy Actuator Package (DAP). The DAP enables field oriented control of the 21 pole pairs at speeds relevant for wearable robotics (~300 rad/s) and uses a PWM frequency of 20 kHz. The DAP includes built-in low level control, including position, current, and impedance control options. Within the drive, position and current feedback loops are closed at 1 kHz and 10 kHz respectively. Onboard sensing includes electrical states of the motor windings and bus, as well as a nine-axis inertial measurement unit (model: MPU-9250, InvenSense, San Jose, CA, USA), temperature sensing, and a 14-bit absolute encoder (model: AS5047P ams AG, Premstaetten, Austria). Motor line to line currents are measured via a 12bit current sensor within the drive and line to line voltages are provided from the drive, obtained by multiplying PWM duty cycle by bus voltage. Depending on the application, peripheral electrical hardware can communicate with the DAP via Bluetooth, Universal Serial Bus (USB), Serial Peripheral Interface (SPI), Inter-Integrated Circuit (I<sup>2</sup>C), and RS-485. The DAP can be used with higher-level control systems to select control type, set controller gains, provide reference signals, and acquire data [5], [6]. Detailed specifications of the motors are described in Table I.

In this paper, the electrical state of the windings is represented using the brushed DC electromechanical model for convenience and simplicity. That is, for our analysis, we converted the 3-phase sinusoidal winding currents and voltages to fictitious direct current and voltage (*i.e.* quadrature quantities). Using the direct-quadrature transformation [11], we report values in terms of the q-axis, which rotates along the rotor shaft. For a sinusoidally wound BLDC motor, this conversion is equivalent to the root-mean-square of the 3-phase currents, and enables discussion of electrical states without including sinusoidally varying voltages and currents.

## A. Efficiency

The efficiency of a motor and drive can be especially important for many applications. Since both power and

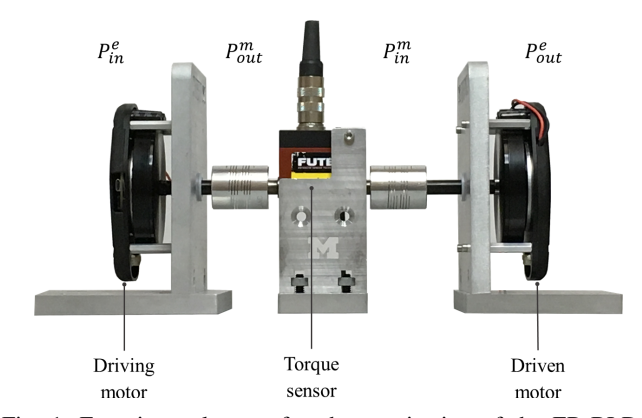


Fig. 1: Experimental setup for characterization of the ER-BLDC motor and drive. Two identical motors were coupled through a common shaft which included a torque sensor. During operation, the driving motor converted electrical power  $(P_{in}^e)$  into mechanical power  $(P_{in}^m)$ , while the driven motor converted mechanical power  $(P_{in}^m)$  into electrical power  $(P_{out}^e)$ .

loss scale with current and velocity in the electrical and mechanical domains, respectively, motor efficiency is dependent on the specific current-voltage regimes of operation (or equivalently, torque-speed regime). To this end, we developed an experimental dynamometer to assess motor and drive efficiency. Two ER-BLDC motors (DAPs) were coupled through a common rotational shaft. A contactless torque sensor was secured within the common rotational shaft (model: TRS605, Futek Advanced Sensor Technology, Inc., Irvine, CA, USA) (Fig. 1). The analog voltage from the torque sensor was acquired by a 16-bit analog to digital converter (model: ADS 1115, Texas Instruments, Dallas, TX, USA), which was recorded using a microcomputer (model: Raspberry Pi 3 Model B, Raspberry Pi Foundation, Cambridge, UK). The microcomputer also communicated via USB to the ER-BLDC drives, acquiring digitized data regarding motor electromechanical state, angular velocity, bus current, winding current, bus voltage, and winding voltage were obtained at 320 Hz, and stored with digitized torque data for post processing. Both motors were powered by a common 36 V lithium polymer (LiPo) battery with a capacity of 950 mAH (model: 25087X2, Venom Power, Rathdrum, ID, USA). In this experiment, one motor operated in positive power (driving motor), while the other motor provided a resistance, operating in negative power (driven motor). The use of two identical motors (driving and driven) enabled quantification of efficiency for two (nearly) opposite currentvoltage conditions for a given current-voltage test. The equations governing the steady state operation of coupled motors are described as follows, converted to the quadraturebased brushed electromechanical model. Applying Newton's Second's Law yields:

Driving: 
$$\mathscr{H} = k_t i_+ - b\dot{\theta} - \tau_L$$
 (1)

Driven: 
$$\cancel{\mathcal{H}} = -k_t i_- - b\dot{\theta} + \tau_L$$
 (2)

where  $i_+$  and  $i_-$  are the q-axis winding currents of driving and driven motor, respectively; J is the rotor's moment of

inertia;  $\dot{\theta}$  is the angular velocity;  $\ddot{\theta}$  is the angular acceleration;  $k_t$  is the q-axis torque constant;  $au_L$  is the load torque, and b is the viscous damping coefficient.  $J\hat{\theta}$  are neglected, since both motors are steady state (i.e. constant velocity).

Using the traditional brushed electromechanical model, winding voltage can be described by applying Kirchoff's Voltage Law:

Driving: 
$$v_{+} = k_{b}\dot{\theta} + i_{+}R + L \frac{d\ell}{dt}$$
 (3)  
Driven:  $v_{-} = -k_{b}\dot{\theta} + i_{-}R + L \frac{d\ell}{dt}$  (4)

Driven: 
$$v_{-} = -k_b \dot{\theta} + i_{-}R + L \frac{d\ell}{dt}$$
 (4)

where  $v_{+}$  and  $v_{-}$  are the q-axis winding voltages applied to driving and driven motor, respectively,  $k_b$  is the back-EMF constant, and R is the phase resistance of the windings. Inductances  $(L\frac{di}{dt})$  are omitted as the motors are at steady state and the q-axis current is a constant value. Finally, it should be noted that the motors were placed face-to-face; thus, the angular velocities had opposite signs, while the torque had a consistent sign.

Efficiencies were investigated across a range of currentvoltage conditions. In general, the driving motor was operated at a fixed, open-loop q-axis voltage across the windings that varied from  $0 \sim 39.2 \text{ V}$  at 2.4 V intervals. In contrast, the driven motor was generally operated in closed-loop current control, with desired q-axis currents ranged from  $0 \sim 19.8$ A at 0.8 A intervals. Tested current-voltage conditions were required to satisfy the inequality:  $v + 3.2i \le 80.8$  where v, i are commanded voltage and current, respectively. In total, 678 combinations of voltage and current sets were tested. For each combination of current and voltage, applied motor voltage was increased linearly for one second, with one second of steady state behavior before the voltage was decreased linearly to zero over an additional one second. Each test was a total a three seconds in duration. Three second duration was chosen to balance the time required to safely reach steady state, while limiting the thermal rise in winding temperature.

To quantify motor power and efficiency, the data were analyzed in MATLAB (The MathWorks, Inc., Natick, MA, USA). The efficiency of driving motor was calculated as:

$$\eta_{+} = \frac{\tau_L \dot{\theta}}{i_{\perp}^b v_{\perp}^b} \tag{5}$$

where  $i_+^b$  is the bus current,  $v_+^b$  is the bus voltage, and their product  $i_+^b \cdot v_+^b$  is the input electrical power, averaged across the one second interval at steady state. The bus power represents the electrical state of the power source (i.e. batteries). Similarly, we calculated the mechanical power as  $\tau_L \cdot \dot{\theta}$ , also averaged across the one second interval. The efficiency of driven motor was quantified as:

$$\eta_{-} = \frac{i_{-}^{b} v_{-}^{b}}{\tau_{L} \dot{\theta}} \tag{6}$$

which is the reciprocal of the driving motor's efficiency, where the motor is driven by the mechanical power from the driving motor, generating electrical power  $(i_-^b \cdot v_-^b)$ . Any

condition where the angular velocity was less than 0.1 rad/s was considered a stall condition, and was not analyzed.

## B. System Identification

1) Torque / Back-EMF constant: A motor's torque (or back-EMF) constant scales the conversion from electrical power to mechanical power of the motor. We completed two tests to obtain estimates of the q-axis torque constant and back-EMF constant separately. To quantify torque constant, the motor's output shaft was mounted to the torque sensor, which was mechanically grounded (i.e. in a stall condition). Current commands were provided to the drive by the microcomputer. Currents were tested from -5 to 5 A at 1.0 A intervals. Each trial had a duration of nine seconds following the onset of torque; first and last one second were removed from analysis to ensure steady state behavior. Five trials were repeated at each current level. Data collected by the microcomputer included desired winding current, measured winding current, and measured torque at a sample rate of 250 Hz. The motor torque and current during each trial were averaged across the seven second trial duration. Subsequently, the data from all trials were averaged to obtain a single current-torque value for each current condition. The torque constant was obtained by linear regression between the average measured torques and average measured winding currents. Goodness of fit was determined by the coefficient of determination (i.e. R-squared).

Similarly, to quantify the back-EMF constant, the motor's angular velocity was measured as a function of applied winding voltages. The motor's rotor was able to spin freely, operating at the no-load speed for each applied voltage. To calculate the back EMF voltage, we subtracted the voltage drop across the winding resistance  $(i \cdot R)$  from the applied voltage, the difference of which is the back-EMF (Eq. 3, 4) during steady state conditions. The motor was operated at a fixed, open-loop voltage across the windings, tested between -22 and 22 V at 5.4 V intervals. Data collection protocol and post-processing procedures were identical to characterization of the torque constant.

2) Inertia and Viscous Loss: The rotor inertia and viscous loss properties have important effects on the dynamic response, especially for ER-BLDC motors, which often have greater rotor inertia values. In this experiment, the two coupled motors interacted, and the interaction dynamics were used to estimate the inertia and viscous loss of the motor. The driven motor had the motor leads open with no control commands present, and thus, acted as a pure inertia and viscous load. To estimate motor properties, we used a nonparametric system identification technique implemented in the frequency domain. The reference position trajectory was provided by the microprocessor, and was a Gaussian random process, low-pass filtered using a third order Butterworth filter with a cutoff frequency of 40 Hz, and was scaled to a peak value of  $\pm$  180°. Five trials were conducted, each with a duration of 60 seconds, with data collected at a sample rate of 250 Hz. Following data collection, MATLAB was used to perform the system identification analyses with an input of load torque and output of angular velocity. The frequency response was determined using Blackman-Tukey spectral analysis—where the auto-spectrum and cross-spectrum are divided in the frequency domain [12], with a window length of 100 samples and an overlap of zero samples. Following estimation of the frequency response, a first-order model was fit to the frequency response data:

$$\frac{\dot{\Theta}(s)}{T_L(s)} = \frac{1}{Js+b} \tag{7}$$

The sum-squared error between the magnitude of the secondorder model and the non-parametric frequency response was calculated in the range of logarithmically spaced frequencies where coherence was greater than 0.85. Coherence values closer to 1.0 indicate linearity between the input and output, supporting our choice to use a linear model across the range of frequencies tested. The parameters for the first-order model (inertia and damping) were chosen that minimize the corresponding error in the frequency response. A single set of inertia and damping values were obtained by averaging the optimized parameters across all trials. The estimated parameters were used to compute the output (angular velocity) of a separate validation dataset, and variance accounted for (VAF) was used to estimate model agreement. Lastly, we repeated the same experiment without the driven motor, thereby measuring any inertia and damping associated with the torque sensor and driving shafts. The inertia and damping of the sensor and shafts were removed from the values obtained using both motors.

Additionally, damping coefficient was measured using a separate experiment investigating the relationship between angular velocity and winding current. Voltages were commanded from -22 to 22 V at 5.4 V intervals to the drive, which corresponded to -160 rad/s to 160 rad/s at 27 rad/s intervals. The current and angular velocity for each set were obtained by averaging the measured current and velocity during seven second duration, and averaged again across the five trials for each set.

# C. Thermal properties

Joule heating of the motor's windings is among the chief limitations of system performance. The flow of heat flux to the environment is governed by a combination of convection and conduction-first order ordinary differential equations (ODEs) that can be modeled in the electrical domain (Fig. 2). To this end, we conducted experiments to quantify the thermal properties of the windings and housing structures of the DAP and the T-motor KV100 separately. We applied 8 A of DC current across two of the three ER-BLDC leads. Data were recorded for 65 minutes, which was known to enable the system to reach a steady state temperature. Two approaches were used to determine the thermal properties, differing in how the temperature of the windings were obtained. First, temperatures were directly acquired by infrared temperature camera (model: FLIR One Pro, Flir System Inc., Wilsonville OR, USA). The temperature of the windings and housing were measured and recorded every minute (1/60 Hz)

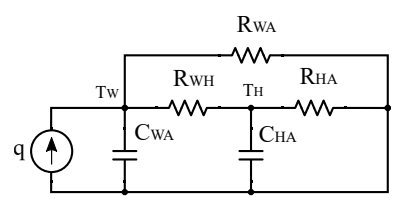


Fig. 2: Analogous electrical circuit of the thermal modeling comprised of thermal resistances and capacitances.

in software. The overall winding temperature was a weighted sum of the two different measured winding temperatures<sup>1</sup>. Second, we recorded the current and voltage applied to the motor using a 16-bit data acquisition system (model: USB-6218, National Instruments Corporation, Austin, TX, USA) sampling at 580 Hz. Measured currents and voltages were used to compute the instantaneous resistance, which is related to the temperature via temperature coefficient of resistivity (TCR) [13]. Thermal resistances and capacitances were obtained by fitting parameters of the first order ODEs relating applied heat flux to temperature rise. Thermal impedances of each motor were obtained by Newton's law of cooling:

$$\frac{Q(s)}{\Delta T(s)} = \frac{1}{R_{WA}} + \frac{1}{R_{WH} + \frac{R_{HA}}{C_{HA}R_{HA}s + 1}} + C_{WA}s \quad (8)$$

where Q is the heat flux,  $R_{WH}$ ,  $R_{HA}$ ,  $R_{WA}$  are thermal resistances of the winding to housing (WH), housing to ambient (HA) and winding to ambient (WA), respectively and  $C_{WA}, C_{HA}$  are capacitances of the winding to ambient and housing to ambient, respectively. We used a genetic algorithm-based optimization routine to minimize the sumsquared error between the measured temperatures acquired by the thermal camera and the temperatures governed by the ODEs from the thermal circuit. The parameters (thermal resistances and capacitances) of the second-order model were chosen that minimizes the error. The steady state temperatures of the windings and housing were obtained by multiplying the heat flux  $(i^2R)$  by the relevant thermal resistance. Note that the heat flux changes as function of time, because the electrical resistance of the windings increases as the temperature rises.

## D. Closed-loop Control

The drive within the DAP includes on-board closed loop control for position and current, the performance of which were assessed in this section. For the position control tests, the motor was able to spin freely; in contrast, for the current control tests, the motors rotor was grounded (as in the previous experiments determined the back-EMF and torque constants). Reference trajectories were provided by the microcomputer at a rate of approximately 725 Hz over USB to the drive.

We conducted step response tests to quantify the closedloop controller performance in the time domain. Reference

<sup>&</sup>lt;sup>1</sup>When current passes between two leads in a delta winding configuration, two windings experience half the current of the third winding; thus, the total heat generated can be calculated as a weighted sum.

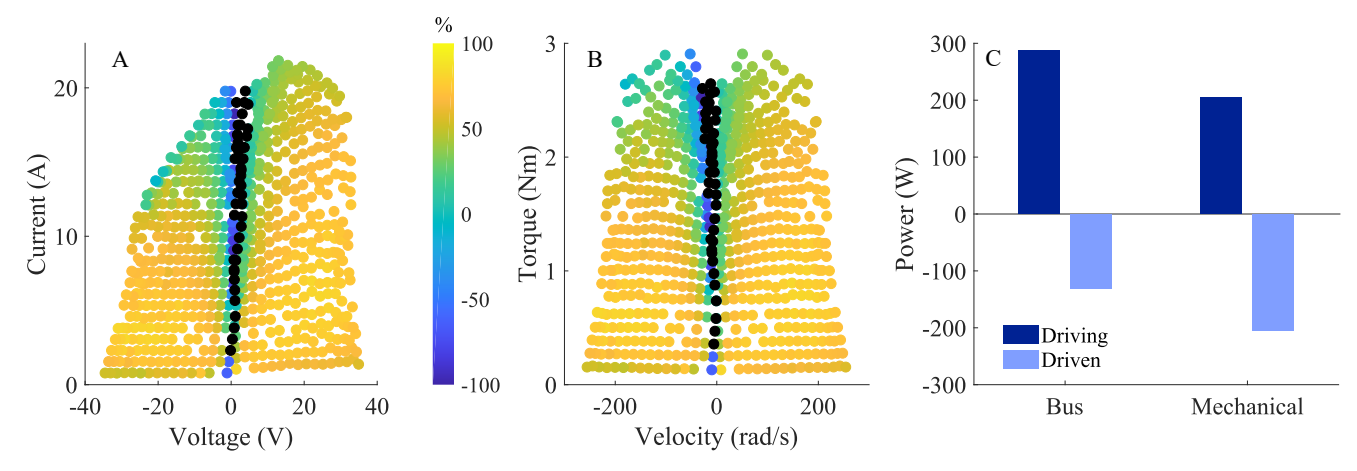


Fig. 3: Total efficiencies (bus electrical power in; mechanical power out) of the actuator in different current and voltage (a) and torque and velocity conditions (b). The yellow color spectrum represents positive efficiency and the blue spectrum shows negative efficiencies. Negative efficiency occurs when the voltage across the winding is larger than back-EMF, and only occurs during negative mechanical power. Efficiencies less than -100% are depicted in black dots. (c) Plot depicts electrical power of the bus (c, left) and mechanical power (c, right) of the motor for the 15.8 A and 24.5 V condition. During each current-voltage condition, one motor operated in positive mechanical power, while the other provided resistance, operating in negative mechanical power. The relationships between the input and output powers provided the ability to assess total efficiency across a range of torque-speed combinations. Note that the mechanical power coupling the two motors is identical.

step inputs were provided at 180°, 360°, and 720° for the position control tests, and 3.3 A, 6.6 A, and 9.9 A for the current control tests (which approximately corresponds to 0.5 Nm, 1 Nm, 1.5 Nm respectively). Each trial had a duration of three seconds and five trials were repeated at each step reference level. Rise time, overshoot, and steady-state error were calculated to quantify controller performance. Subsequently, these values were averaged across all trials and reference levels to obtain single value for each parameter for both the position and current controllers.

We conducted frequency response tests to quantify the closed-loop controller performance in the frequency domain. A Gaussian random process was low-pass filtered using a third order Butterworth filter, which provided the timevarying reference input trajectories. The cutoff frequency of the low-pass filter was 70 Hz and 350 Hz for the position and current control, respectively. The reference trajectories were then scaled to a peak value of 180°, 360°, and 720° for the position control tests; 3.3 A, 6.6 A, and 9.9 A for the current control tests. All trials had a duration of 10 seconds, and five trials were repeated at each reference level. The frequency response was determined using Blackman-Tukey spectral analysis with a window length of 1000 samples. Bandwidth was determined by the frequency where the magnitude crossed -3 dB. Bandwidth values were averaged across all trials and reference levels to obtain single value for the position and current controllers.

## III. RESULTS

## A. Efficiency

Efficiencies of the ER-BLDC motor were calculated across the current-voltage and torque-speed regimes (Fig. 3a, b), with a representative trial shown in Fig. 3c. In general, efficiencies during positive power (quadrant one, >0 V, >0 rad/s) are all greater than zero and over 65%, except during higher current ( $>\sim$ 20 A,  $>\sim$ 2.8 Nm) conditions. During negative power (quadrant two, <0 V, <0 rad/s), both positive and negative efficiencies were observed. Low and negative efficiencies were more prominent at higher current conditions ( $>\sim$ 13 A, >1.8 Nm), but were present across all tested currents at low velocity ( $\sim$ 0V). The mean value of positive efficiencies across all conditions was 56  $\pm$  20 %.

## B. System Identification

- 1) Torque / Back-EMF constant: We observed the characteristic linear relationships between torque and q-axis current, as well as q-axis voltage and angular velocity (Fig. 4b, c). The slope of the line of best fit for the torque-current data (i.e. torque constant) was 0.141 Nm/A with 95% confidence interval (C.I.) of [0.140, 0.142] Nm/A. The R-squared value for the line of best fit was 0.999. The slope of the line of best fit for the voltage-velocity data (i.e. back-EMF constant) was 0.137 V/rad/s (95% C.I.: of [0.135, 0.138] V/rad/s). The R-squared value for the line of best fit was 0.999.
- 2) Inertia and Viscous Loss: The optimized values of inertia and damping coefficients of the second order model across all trials (Eq. 7) were  $1.21\cdot10^{-4}\pm1.95\cdot10^{-6}~{\rm kg}\cdot m^2$  and  $2.6\pm0.35~{\rm mNm/rad/s}$ , respectively. The data fit the model well, with a VAF of 83%. When the model was tested with a separate, validation input, the VAF was also 83%.

The damping property of the motor was also investigated by analyzing the current-angular velocity relationship at noload speed (Fig. 4a). When linear regression was used to estimate the current as a function of positive velocity, the slope was 1.12 mA/rad/s (95% C.I.: [0.41, 1.82] mA/rad/s) and the offset was 65 mA. Using the torque constant and representing these data in terms of torque, the slope was

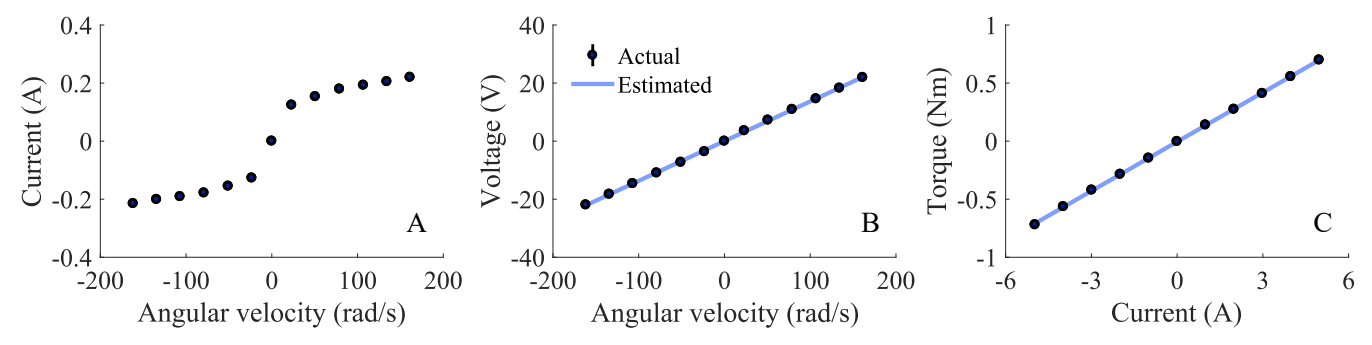


Fig. 4: Plots of no-load current (a), voltage-speed (b), torque-current (c) relationships. The slope of the voltage-speed relationship is the back EMF constant, and the slope of the torque-current relationship is the torque constant. The standard deviations of angular velocities, winding currents and voltage are depicted vertically. Standard deviations for all lines are not visible as their errors are smaller than the scale of both axes. Lines of best fit are shown.

0.16 mNm/rad/s (95% C.I.: [0.06, 0.26] mNm/rad/s) and the offset was 9.1 mNm. The y-axis intercept indicates that the damping behavior of the motor is nonlinear. The R-squared value for the line of best fit was 0.77.

# C. Thermal properties

The thermal responses of both the T-motor (Fig. 5a) and DAP (Fig. 5b) show steep rise in temperature initially, and gradually levels off as they reach steady-state. Measured temperatures of the housing were lower than the winding for both T-motor and the DAP. Temperatures estimated by the ODE (Eq. 8) showed a better agreement with the thermal image data than temperatures estimated by the TCR. The steady state temperature of the DAP (96.9°C) was lower than that of the motor (102.7°C). This discrepancy agrees with the fact that the additional structural mass (7075-T6 Aluminum) of the DAP acted as a heat sink, lowering the thermal resistance.

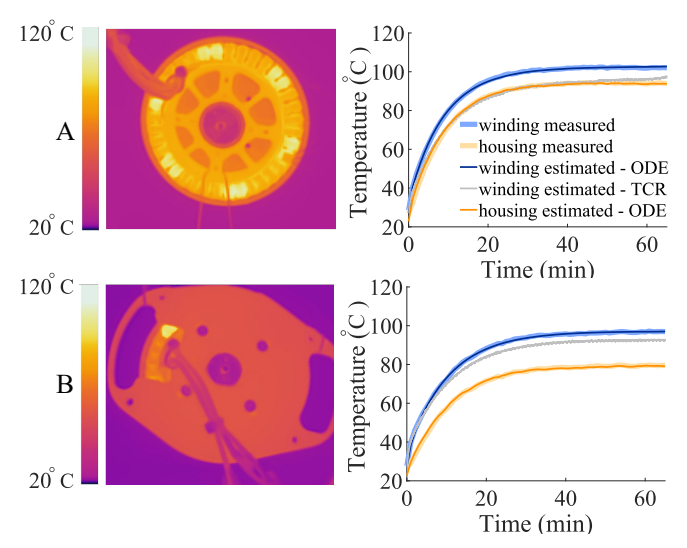


Fig. 5: Infrared thermal image (left) and thermal responses (right) of the T-motor (a) and DAP (b) at steady state. The measured temperatures using the thermal imaging camera; estimated temperatures of the winding and housing using the thermal model (Fig. 2) and TCR are depicted.

## D. Closed-loop Control

Step responses of the current and position feedback control (first row of Fig. 6) show accurate and persistent tracking performance (steady state error < 0.6%) across all reference inputs in time domain. For the position control, the average rise time and settling time across all trials were  $22.2 \pm 6.1$  ms and  $60.3 \pm 14.8$  ms, respectively; for the current control, the rise time and settling time were  $5.0 \pm 0.7$  ms and  $30.2 \pm 16.9$  ms, respectively. Overall, the settling times of both controllers increase as the amplitude of reference step inputs increase. Note that the rise and settling time of the current controller were less than that of the position controller.

Bode plots for magnitude and phase (second and third rows of Fig. 6) shows varying frequency response characteristics of the closed-loop systems at different reference inputs. In general, for the position control, the bandwidths were approximately  $15 \sim 20$  Hz; for the current control, they were greater than 320Hz.

#### IV. DISCUSSION

In this paper, we quantified the time and frequency domain characteristics of a high-performance ER-BLDC motor and the closed-loop control performance of an accompanying brushless drive. The motivation of this paper is to provide accurate and detailed specifications of a common ER-BLDC motor, the parameters of which are often unreported or not generalizable beyond drone applications. We characterized the motor's transfer function, efficiency across torque-speed regimes, as well as thermal properties. Accurate and detailed motor specifications are increasingly important, especially as ER-BLDC motors developed for the drone industry are more commonly used in general robotic applications.

## A. Efficiency

The efficiency pattern across torque-speed and current-voltage regimes were asymmetric about the origin (Fig. 3). For the current-voltage representation, the asymmetry stems, in part, from the x-axis representation of total voltage across the windings, rather than the back-EMF. Thus, for a fixed voltage magnitude and current—that is, two points on either side of the y-axis—the velocities associated with these

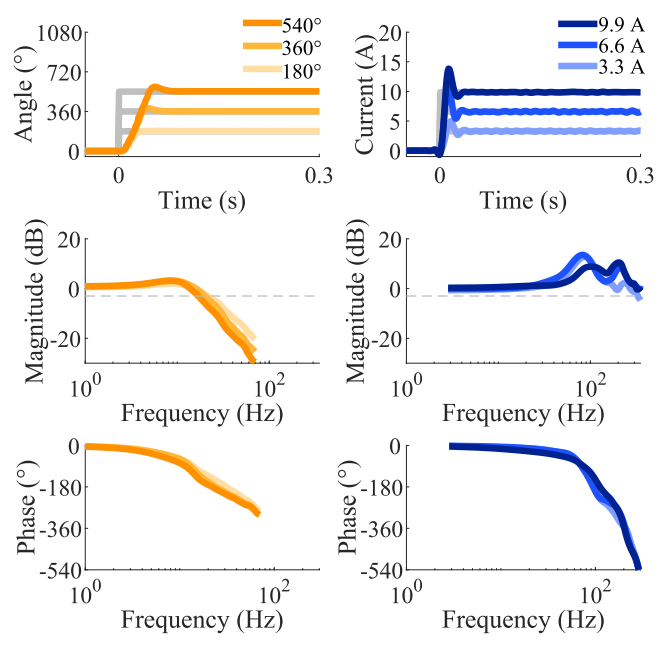


Fig. 6: Position (yellow) and motor current (blue) step responses (first row) and bode plots (second and third row) for the motor. Bandwidth of the motor was determined by the the frequency where the magnitude crossed -3 dB (dashed line).

current  $\pm$ voltage pairs are different (but the voltage drop across the resistance is identical); this mismatch in velocity causes substantially different viscous losses on either side of the current-voltage regions. This also accounts for the right-slanted lean in the negative power quadrant of the current-voltage efficiency plot. Each combination tested at a fixed current has a winding voltage difference of  $2k_b\dot{\theta}$  (Eq. 3, 4). For the torque-speed representation, there is also some asymmetry about the origin. This asymmetry is likely due to the differences in efficiencies of the internal processes within the drive. The conversion of bus voltage to winding voltage is more efficient when the system is operating in positive electrical power, as compared to negative electrical power.

The total efficiency was often less than zero for negative power regimes (this can be observed by the blue spectrum of colors in the efficiency plot (Fig. 3a-b, quadrant two)). Efficiencies less than zero occur in negative power conditions when the voltage drop across the winding resistance is larger than that of the driven motor's back-EMF voltage. In other words, this occurs when the winding current is larger than the maximum current induced from electromagnetic induction:

$$i_{-} > i_{max} = \frac{k_b \dot{\theta}}{R} \tag{9}$$

where the induced maximum current ( $i_{max}$ ) is defined as induced current when the winding voltage is zero (*i.e.* leads are shorted). Alternatively, in terms of electrical power, the power loss across the winding resistance is greater than the mechanical power input. Thus, positive electrical power is required from the power source, leading to an efficiency less than zero. In certain cases, the negative efficiency may be < -100%. This occurs when the power loss across the winding

TABLE I: T-Motor & Dephy Actuator Specifications

	T-motor	Dephy Actuator
Characteristics		
Terminal Resistance (m $\Omega$ )	186	
Terminal Inductance (µH)	138 <sup>a</sup>	
Torque Constant, $k_t$ (Nm/A)	$0.14^{b}$	
Inertia $(g \cdot m^2)$	$0.12 \pm 0.002$	
Damping (mNm/(rad/s))	0.16	
Mechanical Time Constant (ms)	$24.7 \pm 1.2$	
Bus Voltage (V)	36	
Max Continuous Current (A)	7.6 <sup>b</sup>	7.7 <sup>b</sup>
Peak Current - 20 s (A)	23.8 <sup>b</sup>	28.7 <sup>b</sup>
Winding Type	Sinusoidal, Delta	
Thermal		
Thermal Resistance		
Winding-Ambient (K/W)	9861.6	3416.3
Housing-Ambient (K/W)	4.2	3.5
Winding-Housing (K/W)	0.5	1.1
Time Constant Winding (s)	12.9	65.0
Time Constant Motor (s)	548.5	670.6
Control		
Position Steady-state Error (%)		$0.4 \pm 0.2$
Position Rise Time (ms)	$22.2 \pm 6.1$	
Position Settling Time (ms)	$60.3 \pm 14.8$	
Position Overshoot (%)	$8.45 \pm 3.59$	
Position Bandwidth (Hz)		$15 \sim 21$
Current Steady-State Error (%)		$0.6 \pm 0.6$
Current Rise Time (ms)		$5.0 \pm 0.7$
Current Settling Time (ms)		$30.2 \pm 16.9$
Current Overshoot (%)		$39.8 \pm 12.2$
Current Bandwidth (Hz)		> 320
Embedded System		
Commutation Type		FOC
PWM Frequency (kHz)		20
Other Specifications		
Number of Pole Pairs	21	
Number of Phases		3
Product		
Total Weight (g)	240	230°

<sup>&</sup>lt;sup>a</sup> Values reported by Dephy Inc.

resistance is more than twice the mechanical power input.

## B. System Identification

- 1) Torque / Back-EMF constant: In theory, the torque and back-EMF constants are equivalent in the brushed DC model. In our characterization, there was a slight discrepancy (3% error) between these values. This discrepancy may be explained by practical considerations, including that the motor may not be perfectly sinusoidally wounded (i.e. has slight variation in amplitude of phase back-EMF profile), in addition to any noise in the experimental measurements.
- 2) Viscous Loss: Nonlinear friction was observed in current-velocity relationship when the motor was spinning freely (Fig. 4a). This nonlinearity (current-velocity values near the origin) indicates the presence of coulomb friction, with an offset of 65 mA (9.1 mNm). For velocities greater than zero, a constant slope was observed, which indicates a linear model may not fit the data near zero velocity. We used a linear, time invariant approach to estimate the inertia and damping properties separately, and showed strong agreement between output velocity and model-predicted values (VAF:

<sup>&</sup>lt;sup>b</sup> Quadrature quantities

<sup>&</sup>lt;sup>c</sup> Weight excluding the embedded system

83%). This agreement indicates that inertia dominated the torque response, with a limited contribution from the damping component. Using the input velocity and estimated inertia and damping values, the damping component contributed approximately 19% of the output torque and the inertia component contributed approximately 81% of the output torque. Thus, although the damping behavior was nonlinear, the usage of linear methods did not likely affect the analysis.

# C. Thermal properties

Ultimately, a motor's peak performance is limited by its ability to dissipate heat generated by joule heating of the windings. To obtain the thermal characteristics of the motor, current was applied across two leads and we measured the resulting temperature change. These data were used to develop a thermal model, which enables simulation of the rise in winding temperatures for arbitrary current inputs across different robotic applications (assuming the conduction and convection-based thermal resistances do not change appreciably). The thermal model predicts a maximum continuous q-axis current of 7.6 A and 7.7 A; a maximum instantaneous current (for 20 s) of 23.8 A and 28.7 A for the T-motor and DAP, respectively, assuming a maximum permissible winding temperature of 125°C.

## D. Closed-loop Control

The closed loop performance differed substantially between control types (i.e. position control and current control). The position control bandwidth was between 15 - 20 Hz, while the current control bandwidth was greater than 320 Hz. In the time domain, the position control has a consistent velocity during the transient aspect of the step response; that is, response did not vary with step size. This nonlinear behavior stems from the maximum voltage that can be applied, namely, the back-EMF voltage is limited by the power source voltage ( $\sim$ 36 V), known as actuator saturation. The step response for the current control had significant overshoot and a fast rise time (~5 ms), when compared to position control. The increased overshoot can be explained, in part, by the numerator dynamics in the plant's transfer function for current control  $(\frac{I(s)}{V(s)})$ . The faster rise time may be explained by the greater bandwidth of the electrical dynamics, when compared to the mechanical dynamics of the plant  $(\frac{\theta(s)}{V(s)})$ , as well as the lack of saturation.

# E. Comparison to Maxon EC30 4-pole

ER-BLDC motors have several advantages over commonly used motors often designed for "pick and place" automation tasks. In the field of wearable robotics, the Maxon EC30 4-pole is a common motor [14], [15], with a rated power of 200 W and a mass of 300 g. The ER-BLDC motors, such as the T-motor described in this work, have three main advantages: 1) they have a higher torque density, 2) they are more efficient, and 3) they have a better thermal resistance. The high torque density of ER-BLDC motors stems from the larger motor radius, which increases torque by radius squared. A higher torque constant permits a lower transmission ratio, which has

several important advantages, including mass, complexity, efficiency, and controllability. In addition, due to geometric factors, ER-BLDC motors are more efficient. This can be observed by its greater motor constant, when compared to the Maxon EC30 (T-motor:  $0.23 \text{ Nm}/\sqrt{W}$  vs. Maxon EC30:  $0.04 \text{ Nm}/\sqrt{W}$ ). The motor constant describes the thermal loss per unit torque. Finally, ER-BLDC motors may be better at dissipating heat, resulting in a lower thermal resistance. This likely stems from the increase in surface area to volume ratio, which predicts a 28% reduction in thermal resistance, which in actuality, the thermal resistance of the T-motor (4.7 K/W) is 38% less than that of the Maxon (7.6 K/W), where  $R_{WA} \gg R_{HA}, R_{WH}$ .

### ACKNOWLEDGEMENT

The authors would like to thank Dr. Luke Mooney and Mr. Jean-François Duval of Dephy Inc., for their input on approach and support for the DAP.

## REFERENCES

- S. Seok, A. Wang, et al., "Design principles for energy-efficient legged locomotion and implementation on the mit cheetah robot," IEEE/ASME Transactions on Mechatronics, vol. 20, no. 3, pp. 1117– 1129, June 2015.
- [2] G. Kenneally, A. De, and D. E. Koditschek, "Design principles for a family of direct-drive legged robots," *IEEE Robotics and Automation Letters*, vol. 1, no. 2, pp. 900–907, 2016.
- [3] J. W. Sensinger, S. D. Clark, and J. F. Schorsch, "Exterior vs. interior rotors in robotic brushless motors," in *Robotics and Automation* (ICRA), 2011 IEEE International Conference on. IEEE, 2011, pp. 2764–2770.
- [4] M. Motors, "Escon 50/5 servo controller hardware reference," 2013.
- [5] J.-F. Duval and H. M. Herr, "Flexsea: Flexible, scalable electronics architecture for wearable robotic applications," in *Biomedical Robotics* and *Biomechatronics (BioRob)*, 2016 6th IEEE International Conference on. IEEE, 2016, pp. 1236–1241.
- [6] A. F. Azocar, L. M. Mooney, et al., "Design and characterization of an open-source robotic leg prosthesis," in 2018 7th IEEE International Conference on Biomedical Robotics and Biomechatronics (Biorob). IEEE, 2018, pp. 111–118.
- [7] S. Kalouche, "Goat: A legged robot with 3d agility and virtual compliance," in *Intelligent Robots and Systems (IROS)*, 2017 IEEE/RSJ International Conference on. IEEE, 2017, pp. 4110–4117.
- [8] N. Kingry, L. Towers, et al., "Design, modeling and control of a solar-powered quadcopter," in 2018 IEEE International Conference on Robotics and Automation (ICRA). IEEE, 2018, pp. 1251–1258.
- [9] M. A. Tofigh, M. J. Mahjoob, and M. Ayati, "Dynamic modeling and nonlinear tracking control of a novel modified quadrotor," *Interna*tional Journal of Robust and Nonlinear Control, vol. 28, no. 2, pp. 552–567, 2018.
- [10] D. J. Blackman, J. V. Nicholson, et al., "Leg design for running and jumping dynamics," in Robotics and Biomimetics (ROBIO), 2017 IEEE International Conference on. IEEE, 2017, pp. 2617–2623.
- [11] R. H. Park, "Two-reaction theory of synchronous machines generalized method of analysis-part i," *Transactions of the American Institute of Electrical Engineers*, vol. 48, no. 3, pp. 716–727, 1929.
- [12] L. Ljung, "System identification," in Signal analysis and prediction. Springer, 1998, pp. 163–173.
- [13] S. O. Kasap, Principles of electronic materials and devices. McGraw-Hill New York, 2006, vol. 2.
- [14] E. J. Rouse, L. M. Mooney, and H. M. Herr, "Clutchable series-elastic actuator: Implications for prosthetic knee design," *The International Journal of Robotics Research*, vol. 33, no. 13, pp. 1611–1625, 2014.
- [15] M. K. Shepherd and E. J. Rouse, "Design and validation of a torque-controllable knee exoskeleton for sit-to-stand assistance," *IEEE/ASME Transactions on Mechatronics*, vol. 22, no. 4, pp. 1695–1704, 2017.